UC Berkeley
UC Berkeley Previously Published Works

Title

Order–Disorder Transitions in a Polar Vortex Lattice

Permalink

Journal

ISSN

Authors

Zhou, Linming
Dai, Cheng
Meisenheimer, Peter
et al.

Publication Date

DOI

Copyright Information

Peer reviewed

Optimizing Interface Conductivity in Electronics
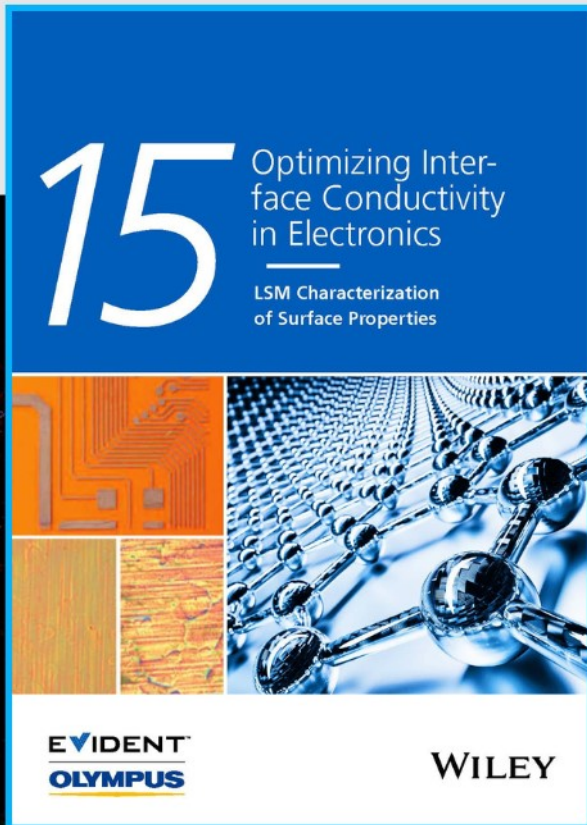
The latest eBook from Advanced Optical Metrology. Download for free.

15 Optimizing Interface Conductivity in Electronics

LSM Characterization of Surface Properties

EVIDENT OLYMPUS

WILEY

Surface roughness is a key parameter for judging the performance of a given material's surface quality for its electronic application. A powerful tool to measure surface roughness is 3D laser scanning confocal microscopy (LSM), which will allow you to assess roughness and compare production and finishing methods, and improve these methods based on mathematical models.

Focus on creating high-conductivity electronic devices with minimal power loss using laser scanning microscopy is an effective tool to discern a variety of roughness parameters.

EVIDENT OLYMPUS

WILEY

Order–Disorder Transitions in a Polar Vortex Lattice

Linming Zhou, Cheng Dai, Peter Meisenheimer, Sujit Das, Yongjun Wu,*
Fernando Gómez-Ortiz, Pablo García-Fernández, Yuhui Huang, Javier Junquera,
Long-Qing Chen,* Ramamoorthy Ramesh,* and Zijian Hong*

Order–disorder transitions are widely explored in various vortex structures in condensed matter physics, that is, in the type-II superconductors and Bose–Einstein condensates. In this study, the ordering of the polar vortex phase in [Pb(Zr$_{0.4}$Ti$_{0.6}$)O$_3$]$_n$/(SrTiO$_3$)$_n$ (PZT/STO) superlattices is investigated through phase-field simulations. With a large tensile substrate strain, an antiorder vortex state (where the rotation direction of the vortex arrays in the neighboring ferroelectric layers are flipped) is discovered for short-period PZT/STO superlattice. The driving force is the induced in-plane polarization in the STO layers due to the large tensile epitaxial strain. Increasing the periodicity leads to antiorder to disorder transition, resulting from the high energy of the head-to-head/tail-to-tail domain structure in the STO layer. On the other hand, when the periodicity is kept constant in short-period superlattices, the order–disorder–antiorder transition can be engineered by mediating the substrate strain, due to the competition between the induction of out-of-plane (due to interfacial depolarization effect) and in-plane (due to strain) polarization in the STO layer. The 3D ordering of such polar vortices is still a topic of significant current interest and it is envisioned that this study will spur further interest toward the understanding of order–disorder transitions in ferroelectric topological structures.

1. Introduction

The order–disorder phase transition is a fundamental physics and materials phenomenon in nature. In condensed matter physics, it has been extensively investigated in a variety of topological systems, including vortices in high-temperature type-II superconductors,[1–3] and rotating Bose–Einstein condensates.[4–6] For instance, it is widely recognized that vortex pinning and thermal fluctuation could lead to the order–disorder transition in the vortex phase of a superconductor, leading to the formation of a vortex glass state,[7] which in turn strongly affects the critical current and threshold magnetic field of the superconducting phase.

In ferroelectric systems, various topological phases such as vortices,[8–15] merons,[16] flux-closure domains,[17–19] spirals,[20] and skyrmions[21–24] have been observed in the low-dimensional ferroelectric heterostructures in recent years. These topological structures usually arise from the complex interplay of charge and lattice degrees of freedom, as well as the depolarization and surface effects within the reduced dimensions. One particular example is the observation of a polar vortex lattice with the continuous rotation of polarization vector surrounding a singularity-like vortex core in the (PbTiO$_3$)$_n$/(SrTiO$_3$)$_n$ (n = 10, 16) (PTO/STO) superlattice systems,[11] akin to the Abrikosov vortex lattice[25,26] observed in the type-II superconductors and ferromagnetic vortices. Previously, Yadav et al.[11] demonstrated that for the polar vortex in the PTO/STO superlattices, while the horizontal long-range order is robust, it has a certain degree of vertical disorder among different PTO layers. This could potentially be a rich area of research that is largely unexplored.[27] One natural question would be: Is it possible to design the vertical order of the polar vortex in the ferroelectric/dielectric superlattice systems?

L. Zhou, Y. Wu, Y. Huang, Z. Hong
Lab of Dielectric Materials
School of Materials Science and Engineering
Zhejiang University
Hangzhou 310027, China
E-mail: yongjunwu@zju.edu.cn; hongzijian100@zju.edu.cn
C. Dai, L. Chen
School of Materials Science and Engineering
Pennsylvania State University
University Park, PA 16802, USA
E-mail: lqc3@psu.edu

The ORCID identification number(s) for the author(s) of this article can be found under https://doi.org/10.1002/adfm.202111392.

P. Meisenheimer, S. Das, R. Ramesh
Department of Materials Science and Engineering
University of California
Berkeley, CA 94720, USA
E-mail: rramesh@berkeley.edu
Y. Wu, Z. Hong
Cyrus Tang Center for Sensor Materials and Applications
State Key Laboratory of Silicon Materials
Zhejiang University
Hangzhou 310027, China
F. Gómez-Ortiz, P. García-Fernández, J. Junquera
Departamento de Ciencias de la Tierra y Física
de la Materia Condensada
Universidad de Cantabria
Cantabria Campus Internacional
Avenida de los Castros s/n, Santander E-39005, Spain

ADVANCED
SCIENCE NEWS
www.advancedsciencenews.com

ADVANCED
FUNCTIONAL
MATERIALS
www.afm-journal.de
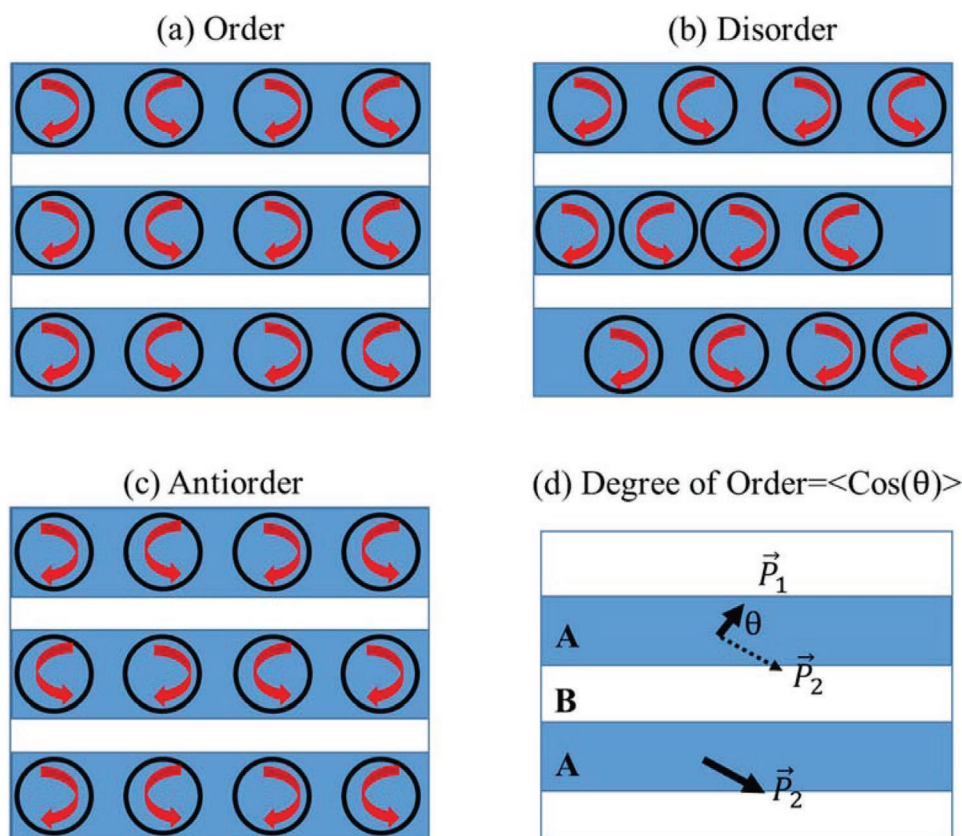
Figure 1. Schematics of different types of vertical order for the vortex system. a) Order, b) disorder, c) antiorder, and d) definition of degree of order. The blue and white regions indicate the ferroelectric and dielectric layers, respectively. A black circle represents one polar vortex, where its rotation direction is indicated by the red arrow. Vertical order and antiorder indicate that vortices in the adjacent layers have the same or opposite rotation directions, while in disorder state there is no long-range correlation between the two layers. The degree of order is defined as the mean value of the cosine of the correlation angle. The degree of order value for the order, disorder and antiorder states is 1, 0, and −1, respectively.

2. Results and Discussion

To address this question, we first define three possible prototypes and establish a parameter (namely the "degree of order") to quantify the vertical order. **Figure 1**a–c shows the schematics of three scenarios for the vertical alignment of the vortex arrays. The ideal, vertically ordered vortex structure is illustrated in Figure 1a, where the vortices in the adjacent ferroelectric layers show the same rotation directions throughout the thickness of the superlattice film. In this scenario, each ferroelectric layer is identical within the superlattice film. In another case, as shown in Figure 1b, the alignment of the vortex along the out-of-plane direction is random, that is, there is barely any long-range vertical order or strong correlation of the vortices in the adjacent ferroelectric layers, giving rise to a disorder, vortex-glass-like state. Figure 1c shows the vertical "antiorder" state, where the rotation direction of the vortex arrays in the neighboring ferroelectric layers are flipped, resulting in alternating clockwise/counterclockwise rotations between the adjacent layers. To further distinguish the three possible states, we define a "degree of order" parameter to quantify the order of the polar vortices (Figure 1d), which is calculated by the mean of the cosine of the angle (θ) between the polarization vectors at the same horizontal position within the ferroelectric in neighboring layers, that is,

$$\cos(\theta) = \vec{P}_1 . \vec{P}_2 = \vec{P}(x, y, z) . \vec{P}(x, y, z + 2n)$$
$$\text{Degree of order} = \langle \cos(\theta) \rangle \tag{1}$$

where n is the superlattice periodicity. The bracket $\langle \rangle$ stands for an average over both (x, y, z) positions in the PZT layers. Under this definition, the degree of order for an ideal order state is 1, while for a completely disorder structure it has a value of 0 and the antiorder state has a degree of order of −1. Thus, this parameter could help to identify the status of the vertical order of the vortex lattice. A similar parameter is also adopted by Takenaka et al. to quantify the degree of correlation in relaxor ferroelectrics.[28] Meanwhile, it should be noted that the degree of correlation in relaxor ferroelectrics is defined over time, while in this case, the degree of correlation is defined over different PZT layers.

Within the perovskite oxide family, to date, such polar textures have been studied almost exclusively in PTO/STO-based superlattices.[11–19,22–24] In this study, the Pb(Zr$_{0.4}$,Ti$_{0.6}$)O$_3$/SrTiO$_3$ (PZT/STO) superlattice is chosen as the model system. The role of isovalent doping in the Ti site (e.g., with Zr^{4+}) is well established through the PZT phase diagram.[29–31] For the Ti-rich part of this phase diagram, the structure remains tetragonal, but exhibits a systematic change in the lattice dimensions with Zr content; particularly, the a-axis of the tetragonal unit cell progressively increases with Zr substitution, while the c-axis

ADVANCED
SCIENCE NEWS
www.advancedsciencenews.com

ADVANCED
FUNCTIONAL
MATERIALS
www.afm-journal.de

decreases, resulting in a decrease in the polarization and increase in dielectric/piezoelectric responses. Thus, within the epitaxial superlattice framework, the PZT system provides a pathway to impose an additional source of strain, namely through the chemical pressure by Zr doping. As compared to the PTO/STO superlattice, PZT and STO have a larger lattice mismatch, which suggests the possibility for a wider strain-tuning window. Whereas the increased lattice constant for the PZT also suggests that the polar vortex could be stabilized with a larger substrate lattice constant as compared to PTO. Furthermore, PZT has a lower Curie temperature and smaller spontaneous polarization with respect to PTO, which suggests a more "flexible" polar state that could possibly be engineered to exhibit various topologies as well as degrees of order within them.

In this work, we investigate via phase-field simulations the phase diagram of the polar structures of PZT/STO superlattices as a function of i) its periodicity when they are assumed to be grown on a $(110)_o$-SmScO$_3$ (SSO) substrate; and ii) when the epitaxial strain is changed from compressive to tensile, keeping the periodicity constant.

The anisotropic in-plane lattice constants of $(110)_o$-SSO substrate are set as 3.991 and 3.983 Å,[32] which causes a compressive strain in the PZT layer and tensile strain in the STO layer (the pseudocubic lattice constants are set as 4.040[33] and 3.905 Å[15] for PZT and STO, respectively). Under this strain condition, an in-plane polarization is induced for the thick STO films, forming single a-domain with polarization pointing toward the in-plane direction (Figure S1a, Supporting Information), in good agreement with previous report.[34] On the other hand, for thick PZT thin films, c-domains are observed with 180° c^+/c^- domain walls (Figure S1b, Supporting Information). The induced polarization for the STO films is ≈0.2 C m^{-2}, while PZT thin films show much larger polarization ≈0.6 C m^{-2} (Figure S1c, Supporting Information).

As a mesoscale simulation tool, phase-field simulation has been widely adopted to study the polar topological structures and topological phase transitions in the ferroelectric heterostructures, and have successfully predicted several topological structures including polar vortices,[11,12] polar merons,[16] polar spirals,[20] and polar skyrmions.[22–24] Our simulations suggest that, on the one hand, for the $(PZT)_n/(STO)_n$ on a $(110)_o$-SSO substrate, a vertical antiorder vortex structure can be engineered with small periodicity (e.g., n = 6), which is triggered by the in-plane polarization in the STO layers induced by the tensile substrate strain. The antiorder to disorder transition is driven by the increase of the periodicity of PZT/STO superlattice on a $(110)_o$-SSO substrate, owing to the increase of c-oriented regions in the PZT layers, as well as to the requirement of reducing the high electrostatic energy associated with the head-to-head/tail-to-tail domain walls in the STO layers. On the other hand, when SSO is replaced by another substrate that imposes a compressive strain, an order vortex lattice state can be formed through the out-of-plane polarization of the STO layer. A strain phase diagram further indicates a strain-mediated order/disorder/antiorder transitions by increasing the in-plane lattice constant of the substrate.

2.1. Influence of the Periodicity for a Constant Epitaxial Strain

The polar structure for the $(PZT)_6/(STO)_6$ superlattice on an SSO substrate is shown in **Figure 2**. Long-range ordered polar vortices with a size of 2 nm form in the PZT layers (Figure 2a,b), similar to the polar vortex lattice observed in the PTO/STO superlattices, which is due to the delicate balance of the elastic, electric, Landau, and gradient energies, as has been discussed in a previous report.[15] The planar view image (Figure 2c) shows the formation of long vortex stripes, with a dislocation-like pattern, consistent with the vortex lattice observed in the PTO/STO system.[15] Notably, it is revealed that the simulated structure exhibits antiorder, where the vortices in the two neighboring PZT layers have opposite rotation directions. This is largely due to the in-plane polarization in the STO layers induced by the tensile substrate strain, which could act as a "gear" where the in-plane polarization directions at the bottom of the vortices in the upper PZT layers share the same polarization directions with the top of the vortices in the lower PZT layers. This geometric confinement triggers the formation of a vertically aligned antiorder vortex structure. Previously, it was also observed that for PTO/STO superlattice on a DSO substrate, such a local in-plane polarization in the STO layer could lead to the formation of local "anti-rotation boundary."[11] However, for the PTO/STO system, the in-plane polarization cannot be formed in every STO layer, so only a few anti-rotation boundaries can be observed, giving rise to a small degree of order. The long-range antiorder alignment with degree of order of −1 has only been predicted in the PZT/STO system so far. Since the in-plane polarization points in opposite directions at consecutive vortices, head-to-head and tail-to-tail domains appear within the STO layer, which costs energy. To minimize the electrostatic energy, the magnitude of the polarization gradually decreases and its direction bends to match the c-domains in the PZT layer. As a result, an antivortex structure (winding number −1) is formed in the STO layer, whose core lies right at the center of the square vortex lattice (Figure 2b). A similar antivortex state has been simulated or observed in ferromagnetic nanostructures (e.g., in Permalloy dot[35] and Fe$_{19}$Ni$_{81}$ thin film[36]), and has also been observed in the short-period PTO/STO superlattice.[14,37]

To further address the role of the STO layers on the rotation patterns and vortex vertical ordering for the PZT layers, the polar structure for $(PZT)_6/(STO)_n$ superlattice on SSO is further investigated (Figure S2–S5, Supporting Information). It can be observed that with the increasing of n, the energy of the head-to-head and tail-to-tail domains increases up to a point where they cannot be stable anymore. At this point (n ≈ 20), a phase transition is observed to form single in-plane a-domains inside the STO layers (Figure S5, Supporting Information). Interestingly, this monodomain phase in the STO precludes the formation of vortices in the PZT layer, as clearly shown by the small density of these singularities in Figure S5, Supporting Information. For an intermediate thickness of STO, the vortex line in the PZT layer rotates by 90°.

We then explore the room temperature phase diagram for $(PZT)_n/(STO)_n$ superlattice epitaxially grown on a $(110)_o$-SSO substrate as a function of the periodicity, (n = 5–30) (**Figure 3**). An antiorder to disorder transition is observed, with the degree of order switching from −1 to 0, with increasing periodicity. The driving force behind this evolution is twofold. First, the larger the periodicity, the higher the electrostatic energy that would be stored in the head-to-head and tail-to-tail domain walls within
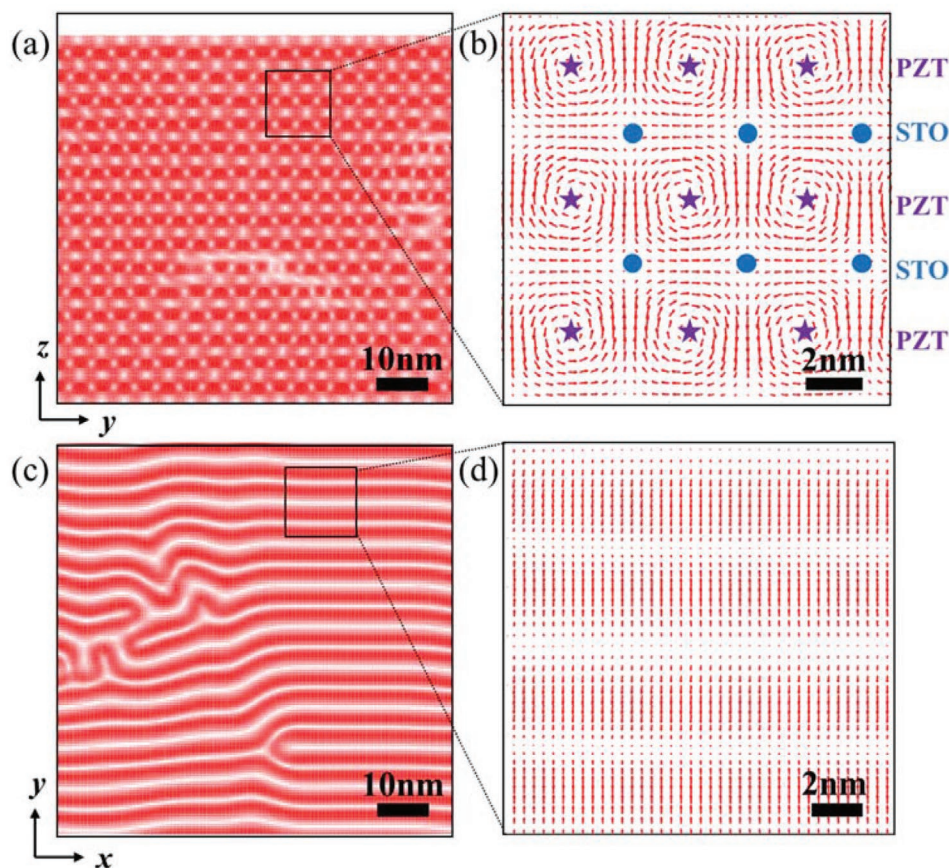
Figure 2. Polar structure for the $(PZT)_6/(STO)_6$ on a SSO substrate. a) Cross-section view of the polar vector, showing the alignment of the polar vortices. b) Zoom-in view. The core of the antivortex within the STO layer is marked with a blue dot, while the vortex core is marked with purple star. c) Planar view on the top PZT layer, showing the formation of vortex stripes and dislocation patterns. d) Magnified view of the planar view of the vortex stripes.

the STO layer. One way to release this electrostatic energy is to tilt these domain walls, in such a way that the polarization charge is reduced. This is observed in Figure 3b for $n = 16$, and translates into the fact that the in-plane components of the

polarization within the STO layer connect vortices that are not aligned along the z-direction. Second, the larger the periodicity, the larger the out-of-plane polarization within the PZT layer. Indeed, for short-period superlattices ($n = 6$), P_z in the PZT
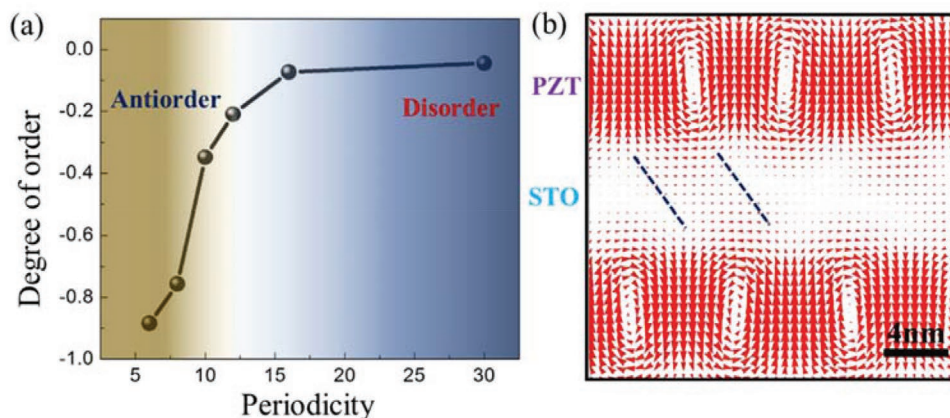
Figure 3. Periodicity phase diagram for $(PZT)_n/(STO)_n$ ($n = 5$–30) superlattice on a SSO substrate. a) Degree of order as a function of periodicity, demonstrating the thickness-driven antiorder/disorder transition, dark yellow region indicates the antiorder structure, while dark blue shows the formation of disorder structure, where the light color demonstrates the transitional state in between a fully antiorder and disorder state. b) Disorder structure for large periodicity $n = 16$. The blue dashed lines mark the tilting of the head-to-head and tail-to-tail domain walls.

ADVANCED
SCIENCE NEWS
www.advancedsciencenews.com

ADVANCED
FUNCTIONAL
MATERIALS
www.afm-journal.de

layer is greatly suppressed, of the same magnitude as the strain-induced in-plane polarization in the STO layer (≈ 0.2 C m^{-2}). For higher periodicities ($n = 16$; Figure 3b), the shape of the vortices has changed to a more rectangular domain wall type, while P_z within the PZT layer increases up to ≈ 0.4 C m^{-2}, with a concomitant increase of the coupling with the out-of-plane polarization in the STO layer (Figure S6b, Supporting Information). Therefore, to minimize the gradient of the polarization along the z-direction and the formation of polarization charges, there is a tendency to align the up/down domains in the PZT and the STO layer, favoring the appearance of a more ordered phase, and reducing the average value of the cosine shown in Figure 1 from its initial value of −1. For very large periodicities, the out-of-plane polarization within the STO layers cannot be maintained, and the PZT layers are completely decoupled, leading to the phase coexistence of vortex and small c-domains (≈ 5 nm). Whereas no long-range phase coexistence with large c-domains and vortex has been observed so far, which could be because the large-scale c-domain is very unstable in the context of a (PZT)$_n$/(STO)$_n$ superlattice (i.e., $n < = 20$) with a large depolarization field. It should be noted here that for short-period (PTO)$_n$/(STO)$_n$ superlattices on DSO, that is, $n = 6$, due to the large depolarization effect, the a_1/a_2 twin structure is the most stable one.[15] Meanwhile, with the reduced polarization and Curie temperature, the polarization is softer in the PZT

systems, which could favor the polarization rotation and vortex formation even with short periodicity.

2.2. Influence of the Epitaxial Strain for a Constant Periodicity

Since the polarization in the STO layer plays an important role in determining the degree of order, it can be expected that the epitaxial strain could be a key factor to tune it. The strain versus degree of order diagram with fixed small periodicity ($n = 6$) is plotted in **Figure 4**. To simplify the model, biaxial strain with a cubic substrate is assumed afterward unless otherwise specified. Three distinct regions can be distinguished. When the substrate lattice constant is small (<3.960 Å), an order structure can be observed with a degree of order close to 1. With increasing of the substrate lattice constant (from 3.960 to 3.975 Å), the compressive strain in the PZT layers decreases while the tensile strain in the STO layers increases, giving rise to the disordered state with a degree of order close to 0. Further increasing of the substrate lattice constant leads to the formation of an antiorder state, where the degree of order is close to −1.

When the PZT layer is under a large compressive strain, the out-of-plane polarization determines the physical behavior of the superlattice. The polarization pattern in Figure 4b shows
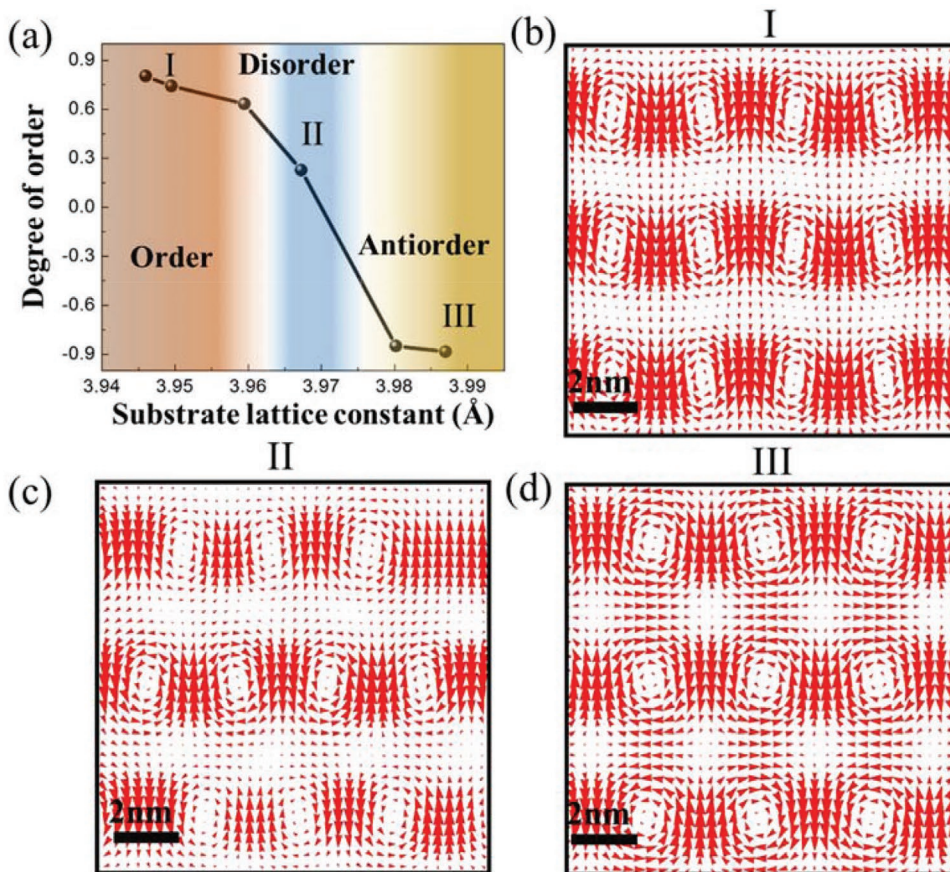
Figure 4. Strain phase diagram for (PZT)$_6$/(STO)$_6$ superlattice. a) The degree of order as a function of substrate in-plane lattice constant, indicating the formation of three different phases, that is, order, disorder, and antiorder states. b) Order state with substrate lattice constant of 3.95 Å. c) Disorder state with substrate lattice constant of 3.966 Å. d) Antiorder state with substrate lattice constant of 3.987 Å.

the order structure where the vortices in the neighboring PZT layers rotate in the same direction. A finite out-of-plane polarization is observed in the STO layers, avoiding the discontinuity in the polarization and the appearance of electrostatically expensive bound charges. It shares the same out-of-plane polarization direction with the upper and lower PZT layers, thus tuning the order alignments of the vortices in the whole superlattice system. Meanwhile, an antivortex state is also shown in the STO layers, perfectly aligned with the vortex cores.

When the in-plane lattice constant is large enough, the compressive strain on the PZT layer is reduced and the epitaxial strain on the STO increases. The in-plane component of the polarization is the main physical ingredient to determine the ground state of the system. As already discussed in Figure 2, the antiorder structure is the most stable phase, as seen in Figure 4d, with the antivortex in the STO layer now located midway between two consecutive vortices. The temperature stability of the order and antiorder vortex structure is further investigated. As shown in Figure S7, Supporting Information, for the $(PZT)_6/(STO)_6$ superlattices on both SSO and DSO substrates, with increasing temperature, the magnitude of polarization gradually decreases before vanishing at the Curie temperature, leading to the antiorder/order vortex phase to paraelectric phase transition. With the SSO substrate, the phase transition to paraelectric phase occurs at 450 K, while on a DSO substrate, it increases to ≈650 K. This can be understood since a large compressive strain is generated on the PZT layer with DSO substrate, leading to the increase of both the polarization and Curie temperature. Interestingly, well below the Curie temperature, the phase coexistence of the vortex and paraelectric phase is observed for both the antiorder and order structure, indicating the gradual loss of the degree of order through the formation of phase mixtures with paraelectric phase close to the Curie temperature.

In the intermediate regime, a compromise between the two previous scenarios is found. It can be shown how the polarization in STO layers tilts, which is neither horizontal nor perpendicular. The tilting of polarization is largely due to the competition of strain effect (which tends to orient the polarization in the in-plane direction with tensile strain) and the poling effect by the PZT layer (which tends to orient the polarization to the out-of-plane direction). As shown in Figure 4c and Figure S8, Supporting Information, in this case vortices in the neighboring ferroelectric layers can have both order, antiorder, and weak correlation regions, which forms a vortex-glass-like state with only short-range ordering.

To gain physical insights into the strain-induced order–disorder–antiorder phase transition, the energetics of the five different states (c-domain, a-domain, order, disorder, and antiorder states) with varying substrate lattice constants are investigated. As shown in **Figure 5**a, the relative total energy density (defined as the total energy density of the polar state minus the total energy density of the centrosymmetric paraelectric state) of the a-domain structure decreases with increasing substrate lattice constant, while an opposite trend is observed with the other four structures. This can be expected since the c-domain is only favored under compressive strain, while the a-domain is favored at the tensile strain side. It can be observed that the c-domain and centrosymmetric paraelectric
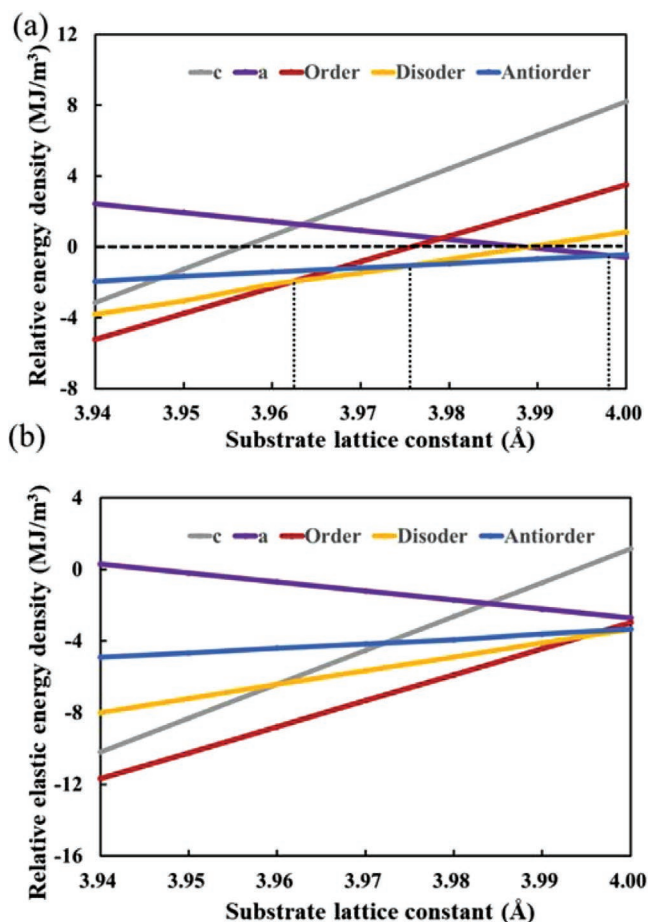
Figure 5. Energetics of the strain-mediated phase transitions for $(PZT)_6/(STO)_6$ superlattice. a) The relative total energy density and b) relative elastic energy density as a function of substrate strain. It is indicated that the order, disorder, antiorder, and a phase are thermodynamically more stable with substrate lattice constant below 3.963 Å, from 3.963 to 3.975 Å, between 3.975 and 3.997 Å, and above 3.997 Å, respectively. The centrosymmetric state is taken as the reference state with zero energy density, marked with dashed line in (a).

phase (zero energy state) is thermodynamically unstable with a substrate lattice constant from 3.94 to 4.00 Å. Whereas the other four curves intersect with each other, giving rise to four thermodynamically favorable polar states under different strain conditions, that is, the ordered vortex structure has a lower energy density when the substrate lattice constant is less than 3.963 Å, followed by the disordered structure from 3.963 to 3.975 Å, the lower energy state with larger substrate lattice parameter (above 3.997 Å) is the a-domain state, whereas the antiorder state is more favorable in between (3.975 to 3.997 Å). The increase in the relative energy density can be understood by further plotting the relative elastic energy (Figure 5b), which shows a similar trend with the same slope as the total energy for the three states since the other energies are insensitive to the strain condition. Interestingly, the order structure is elastically favorable over a larger strain range (i.e., with substrate lattice constant smaller than 3.99 Å). The other energy densities (e.g., electric, Landau, and gradient energy densities) are given in Table S1, Supporting Information. It is clearly shown that the

sum of energies other than elastic energy densities is higher for the order structure, followed by the disorder state. Thus the stable order structure is expected only at a lower substrate lattice constant range. The higher electric energy of the order structure is due to the formation of electrically unfavorable *c*-like regions in the STO layers. Whereas the larger gradient energy density of the order state is a result of the higher density of vortex arrays.

The relative elastic energy densities of the PZT and STO layers are separated (Figure S9, Supporting Information). It is shown that in the PZT layers, all three states show an increase in the relative elastic energy densities with an increase in the substrate lattice parameter. A larger slope is observed for the order phase since the polarization in this phase is larger than in other phases. On the other hand, for the STO layers, the order phase shows an increase in the relative elastic energy since the *c*-type domain is not elastically favorable for STO layers with large tensile strain. Meanwhile, the large in-plane polarization could lower the elastic energy of the STO layers, giving rise to a lowering of the elastic energy in these layers for the antiorder and the disorder states. Since the polarization in the STO layers is relatively small, the eigenstrains (defined as the phase transition strain due to the electrostriction effect) of the STO layers are also correspondingly smaller, showing a smaller slope in the decreasing trend of the elastic energy in these layers.

Finally, the experimental feasibility of the PZT/STO superlattice is discussed. There are several challenges for the experimental synthesis of the PZT/STO systems, including the concise control of the Zr/Ti ratio, the formation of defects such as dislocations and surface buckling[38] for the relaxation of the large substrate strain, as well as the characterization limit to determine the polarization vector with reduced magnitude. Previously, PZT-based superlattice systems have been synthesized experimentally,[38,39] indicating that the experimental growth of the high-quality PZT/STO superlattice to verify the theoretical prediction is highly feasible. In particular, PZT/STO multilayer structures have been grown on an STO substrate and exhibit bubble structures,[39] akin to the polar skyrmion structure observed in the PTO/STO superlattice system, showing the similarity of the PZT/STO system with the PTO/STO system and the possibility to engineer topological phases in the PZT/STO superlattice systems.

3. Conclusion

In conclusion, we investigated the polar structure in the $(PZT)_n/(STO)_n$ superlattice systems through phase-field simulations. An antiorder state is revealed for short periodicity superlattice on an SSO substrate, where the vortices in the neighboring layers anti-align with each other, resulting from the in-plane polarization in STO layers due to the large tensile strain. An antivortex emerges within STO located in between two consecutive vortices. Increasing the periodicity leads to the antiorder to disorder transition, owing to the tilt of the domains of the head-to-head and tail-to-tail domains within the STO layer. Keeping the periodicity of the superlattice constant and sufficiently small, a strain-mediated order–disorder–antiorder transition is revealed, due to the intimate competition between the induction

of out-of-plane (due to interfacial coupling) and in-plane (due to strain) polarizations in the STO layer. We hope this study could spur further interest toward the understanding of order–disorder transitions for ferroelectric topological structures.

4. Experimental Section

Phase-Field Simulation: The spontaneous polarization vector ($\vec{P}_i, i = 1, 3$) was chosen as the order parameter, governed by the time-dependent Ginzburg–Landau (TDGL) equation:[40–42]

$$\frac{\partial \vec{P}_i}{\partial t} = -L \frac{\delta F}{\delta \vec{P}_i} (i = 1, 3) \tag{2}$$

where t is the evolution time, L is the kinetic coefficient related to the mobility of the ferroelectric domain wall, F is the total free energy of the system which has the contribution from the Landau chemical, elastic, electrostatic, and polarization gradient energies, namely:

$$F = \int \left(f_{Landau} + f_{elastic} + f_{electric} + f_{gradient} \right) dV \tag{3}$$

Detailed descriptions of the individual energies can be found in previous reports.[15,40–43] The material parameters (including Landau potentials, elastic constants, and background dielectric constant) were adopted from previous literature.[15,29–31,44–46] For the sake of simplicity, the potential order–disorder of the Zr/Ti ions was ignored in the present work. The simulation temperature for all the studies was set as 300 K. A 3D mesh of $200 \times 200 \times 250$ grids was established, with each grid point representing 0.4 nm. A periodic boundary condition was applied along the in-plane dimensions while the superposition method was applied along the out-of-plane dimension.[47] Along the thickness direction, the whole film was composed of 30 grid points of the substrate, 192 grid points of the (PZT/STO) film, and 28 grid points of air, respectively. The mechanical boundary condition of a thin film was applied, where the displacement at the bottom of the system was fixed to zero, while the out-of-plane stress on the top of the film was fixed to zero.[41] To account for the elastic inhomogeneity of the superlattice system, an iteration-perturbation method was used.[48] A short-circuit electric boundary condition was used, that is, the electric potential at the top and bottom of the film was set to zero.[43]

Statistical Analysis: In the phase-field simulations, for the sake of convenience, the dimensionless variables were employed where the polarization P was normalized by $P_0 = 0.757$ C m^{-2}; all the energy density terms and elastic stress were normalized by $a_0 P_0^2$, where $a_0 = 1.725 \times 10^8$ m^2 N C^{-2}; while the driving forces are normalized by $a_0 P_0$; the spacing was normalized by $l_0 = 1$ nm. Each polar structure in Figures 2–4 of the main text was repeated at least three times with different initial random noises.

Supporting Information

Supporting Information is available from the Wiley Online Library or from the author.

**ADVANCED
SCIENCE NEWS**

www.advancedsciencenews.com

**ADVANCED
FUNCTIONAL
MATERIALS**

www.afm-journal.de

Conflict of Interest

The authors declare no conflict of interest.

Data Availability Statement

The data that support the findings of this study are available from the corresponding author upon reasonable request.

Keywords

[1] G. Blatter, M. V. Feigel'man, V. B. Geshkenbein, A. I. Larkin, V. M. Vinokur, *Rev. Mod. Phys.* **1994**, *66*, 1125.

[2] J. A. Sánchez, R. C. Maldonado, N. R. Cejas Bolecek, G. Rumi, P. Pedrazzini, M. I. Dolz, G. Nieva, C. J. V. D. Beek, M. Konczykowski, C. D. Dewhurst, R. Cubitt, A. B. Kolton, A. Pautrat, Y. Fasano, *Commun. Phys.* **2019**, *2*, 143.

[3] G. Pasquini, D. P. Daroca, C. Chiliotte, G. S. Lozano, V. Bekeris, *Phys. Rev. Lett.* **2008**, *100*, 247003.

[4] J. R. Abo-Shaeer, C. Raman, J. M. Vogels, W. Ketterle, *Science* **2001**, *292*, 476.

[5] W. V. Pogosov, K. Machida, *Phys. Rev. A* **2006**, *74*, 023622.

[6] W. Wang, P. G. Kevrekidis, *Phys. Rev. E* **2015**, *91*, 032905.

[7] M. P. A. Fisher, *Phys. Rev. Lett.* **1989**, *62*, 1415.

[8] S. Das, Z. Hong, M. Mccarter, P. Shafer, Y.-T. Shao, D. A. Muller, L. W. Martin, R. Ramesh, *APL Mater.* **2020**, *8*, 120902.

[9] I. I. Naumov, L. Bellaiche, H. Fu, *Nature* **2004**, *432*, 737.

[10] S. Prosandeev, I. Ponomareva, I. Naumov, I. Kornev, L. Bellaiche, *J. Phys.: Condens. Matter* **2008**, *20*, 193201.

[11] A. K. Yadav, C. T. Nelson, S. L. Hsu, Z. Hong, J. D. Clarkson, C. M. Schlepütz, A. R. Damodaran, P. Shafer, E. Arenholz, L. R. Dedon, D. Chen, A. Vishwanath, A. M. Minor, L. Q. Chen, J. F. Scott, L. W. Martin, R. Ramesh, *Nature* **2016**, *530*, 198.

[12] Z. Hong, S. Das, C. Nelson, A. Yadav, Y. Wu, J. Junquera, L.-Q. Chen, L. W. Martin, R. Ramesh, *Nano Lett.* **2021**, *21*, 3533.

[13] K. Du, M. Zhang, C. Dai, Z. N. Zhou, Y. W. Xie, Z. H. Ren, H. Tian, L. Q. Chen, G. Van Tendeloo, Z. Zhang, *Nat. Commun.* **2019**, *10*, 4864.

[14] A. Y. Abid, Y. Sun, X. Hou, C. Tan, X. Zhong, R. Zhu, H. Chen, K. Qu, Y. Li, M. Wu, J. Zhang, J. Wang, K. Liu, X. Bai, D. Yu, X. Ouyang, J. Wang, J. Li, P. Gao, *Nat. Commun.* **2021**, *12*, 2054.

[15] Z. Hong, A. R. Damodaran, F. Xue, S.-L. Hsu, J. Britson, A. K. Yadav, C. T. Nelson, J.-J. Wang, J. F. Scott, L. W. Martin, R. Ramesh, L. Q. Chen, *Nano Lett.* **2017**, *17*, 2246.

[16] Y. J. Wang, Y. P. Feng, Y. L. Zhu, Y. L. Tang, L. X. Yang, M. J. Zou, W. R. Geng, M. J. Han, X. W. Guo, B. Wu, X. L. Ma, *Nat. Mater.* **2020**, *19*, 881.

[17] Y. L. Tang, Y. L. Zhu, X. L. Ma, A. Y. Borisevich, A. N. Morozovska, E. A. Eliseev, W. Y. Wang, Y. J. Wang, Y. B. Xu, Z. D. Zhang, S. J. Pennycook, *Science* **2015**, *348*, 547.

[18] J. J. P. Peters, G. Apachitei, R. Beanland, M. Alexe, A M. Sanchez, *Nat. Commun.* **2016**, *7*, 13484.

[19] X. Li, C. Tan, C. Liu, P. Gao, Y. Sun, P. Chen, M. Li, L. Liao, R. Zhu, J. Wang, Y. Zhao, L. Wang, Z. Xu, K. Liu, X. Zhong, J. Wang, X. Bai, *Proc. Natl. Acad. Sci. USA* **2020**, *117*, 18954.

[20] Z. Hong, L. Q. Chenn, *Acta Mater.* **2019**, *164*, 493.

[21] Y. Nahas, S. Prokhorenko, L. Louis, Z. Gui, I. Kornev, L. Bellaiche, *Nat. Commun.* **2015**, *6*, 8542.

[22] Z. Hong, L. Q. Chen, *Acta Mater.* **2018**, *152*, 155.

[23] S. Das, Y. L. Tang, Z. Hong, M. A. P. Gonçalves, M. R. Mccarter, C. Klewe, K. X. Nguyen, F. Gómez-Ortiz, P. Shafer, E. Arenholz, V. A. Stoica, S.-L. Hsu, B. Wang, C. Ophus, J. F. Liu, C. T. Nelson, S. Saremi, B. Prasad, A. B. Mei, D. G. Schlom, J. Íñiguez, P. García-Fernández, D. A. Muller, L. Q. Chen, J. Junquera, L. W. Martin, R. Ramesh, *Nature* **2019**, *568*, 368.

[24] S. Das, Z. Hong, V. A. Stoica, M. A. P. Gonçalves, Y. T. Shao, E. Parsonnet, E. J. Marksz, S. Saremi, M. R. Mccarter, A. Reynoso, C. J. Long, A. M. Hagerstrom, D. Meyers, V. Ravi, B. Prasad, H. Zhou, Z. Zhang, H. Wen, F. Gómez-Ortiz, P. García-Fernández, J. Bokor, J. Íñiguez, J. W. Freeland, N. D. Orloff, J. Junquera, L. Q. Chen, S. Salahuddin, D. A. Muller, L. W. Martin, R. Ramesh, *Nat. Mater.* **2021**, *20*, 194.

[25] R. P. Huebener, *J. Supercond. Novel Magn.* **2019**, *32*, 475.

[26] A. A. Abrikosov, *Phys. Today* **1973**, *26*, 56.

[27] V. A. Stoica, N. Laanait, C. Dai, Z. Hong, Y. Yuan, Z. Zhang, S. Lei, M. R. Mccarter, A. Yadav, A. R. Damodaran, S. Das, G. A. Stone, J. Karapetrova, D. A. Walko, X. Zhang, L. W. Martin, R. Ramesh, L.-Q. Chen, H. Wen, V. Gopalan, J. W. Freeland, *Nat. Mater.* **2019**, *18*, 377.

[28] H. Takenaka, I. Grinberg, S. Liu, A. M. Rappe, *Nature* **2017**, *546*, 391.

[29] M. J. Haun, E. Furman, S. J. Jang, L. E. Cross, *Ferroelectrics* **1989**, *99*, 13.

[30] M. J. Haun, Z. Q. Zhuang, E. Furman, S. J. Jang, L. E. Cross, *Ferroelectrics* **1989**, *99*, 45.

[31] M. J. Haun, E. Furman, S. J. Jang, L. E. Cross, *Ferroelectrics* **1988**, *99*, 63.

[32] R. Uecker, B. Velickov, D. Klimm, R. Bertram, M. Bernhagen, M. Rabe, M. Albrecht, R. Fornari, D. G. Schlom, *J. Cryst. Growth* **2008**, *310*, 2649.

[33] C. Chung, *Microstructural Evolution in Lead Zirconate Titanate (PZT) Piezoelectric Ceramics*. Doctoral Dissertation, University of Connecticut **2014**.

[34] G. Sheng, Y. L. Li, J. X. Zhang, S. Choudhury, Q. X. Jia, V. Gopalan, D. G. Schlom, Z. K. Liu, L. Q. Chen, *Appl. Phys. Lett.* **2010**, *96*, 232902.

[35] A. Lyberatos, S. Komineas, N. Papanicolaou, *J. Appl. Phys.* **2011**, *109*, 023911.

[36] G. Minori, N. Yukio, S. Koji, *Jpn. J. Appl. Phys.* **2015**, *54*, 023001.

[37] P. Aguado-Puente, J. Junquera, *Phys. Rev. B* **2012**, *85*, 184105.

[38] M. Gharbi, C. Davoisne, F. Le Marrec, L. Dupont, N. Lemée, *Mater. Lett.* **2020**, *275*, 128138.

[39] Q. Zhang, L. Xie, G. Liu, S. Prokhorenko, Y. Nahas, X. Pan, L. Bellaiche, A. Gruverman, N. Valanoor, *Adv. Mater.* **2017**, *29*, 1702375.

[40] L.-Q. Chen, *J. Am. Ceram. Soc.* **2008**, *91*, 1835.

[41] Y. L. Li, S. Y. Hu, Z. K. Liu, L. Q. Chen, *Acta Mater.* **2002**, *50*, 395.

[42] Z. Hong, J. Britson, J. M. Hu, L.-Q. Chen, *Acta Mater.* **2014**, *73*, 75.

[43] Y. L. Li, S. Y. Hu, Z. K. Liu, L. Q. Chen, *Appl. Phys. Lett.* **2002**, *81*, 427.

[44] A. K. Tagantsev, *Ferroelectrics* **2008**, *375*, 19.

[45] Y. Zheng, C. H. Woo, *Nanotechnology* **2009**, *20*, 075401.

[46] Y. Zheng, C. H. Woo, *Appl. Phys. A* **2009**, *97*, 617.

[47] L. Q. Chen, J. Shen, *Comput. Phys. Commun.* **1998**, *108*, 147.

[48] J. J. Wang, X. Q. Ma, Q. Li, J. Britson, L.-Q. Chen, *Acta Mater.* **2013**, *61*, 7591.